RADIO SCIENCE, VOL. 40, RS6005, doi:10.1029/2004RS003112, 2005

Posterior distributions of a statistic of propagation loss inferred from radar sea clutter

L. Ted Rogers and Michael Jablecki

Atmospheric Propagation Branch, Space and Naval Warfare Systems Center, San Diego, California, USA

Peter Gerstoft

Marine Physical Laboratory, University of California, San Diego, La Jolla, California, USA

Received 18 June 2004; revised 19 April 2005; accepted 18 July 2005; published 18 November 2005.

[1] The generation of a posteriori distribution of a statistic of propagation loss conditioned on observed radar sea clutter is described. The statistic u is the 20th percentile level of the two-way propagation loss at a 5-m height over the 10–60 km range interval. A discrete implementation of the Bayesian paradigm is employed. The forward mapping from the space of environmental parameters into the space of radar clutter incorporates a random process model such that many realizations of modeled clutter are generated for each environmental refractivity parameter combination. The algorithm is adjusted such that over a series of simulated inversion runs, it is seen that for intervals between percentile levels (e.g., between the 20th and 80th percentile levels), a posteriori distributions of u contain the ground truth values of u the correct percentage of the time (60% for the used interval). For real data cases, it is observed that the a posteriori distributions are too narrow. The inversion algorithm is used to examine the behavior of the a posteriori distribution as the noise floor is raised. An abrupt reduction in the information obtained from the clutter (indicated by a widening of the a posteriori distribution) occurs when peak clutter levels over the ranges of 25–50 km drop below about 15 dB for both simulated and real data cases.

Citation: Rogers, L. T., M. Jablecki, and P. Gerstoft (2005), Posterior distributions of a statistic of propagation loss inferred from radar sea clutter, *Radio Sci.*, *40*, RS6005, doi:10.1029/2004RS003112.

1. Introduction

[2] Nonstandard atmospheric refractivity structures significantly affect the performance of shipboard radar systems in the detection of low-altitude targets. The refractivity structure associated with the marine atmospheric surface layer often provides a thin (a few meters to a few tens of meters) and leaky "evaporation duct" that results in up to a factor of 2 extension in detection ranges over what would be expected with a standard atmosphere. The refractivity profile of the surface layer is often characterized by a single parameter, the evaporation duct height δ. The term "surface-based duct" is usually associated with anomalous refractivity structures that are formed by inversion layers or internal boundary layers (i.e., the result of the offshore flow of a relatively hot and dry planetary boundary layer [*Gossard and Strauch*, 1983]). Surface-based ducts are associated with clutter rings and instances where shorelines can be observed using shipboard radars from 200 km or more. The refractivity profiles associated with surface-based ducts are complex in both the vertical and horizontal dimensions and are difficult to characterize in just a few parameters.

[3] Beginning in roughly 1980, the ability to model these effects led designers to incorporate consideration of them in system analysis [*Hitney et al.*, 1985]. By the mid-1990s, systems were being demonstrated for near-real-time shipboard capability for characterization of atmospheric refractivity and its associated impact on radars [*Rowland et al.*, 1996]. At that time, the obvious choice for characterizing refractivity was to use the bulk method [*Liu et al.*, 1979] for characterization of the atmospheric surface layer. Radiosondes, rocketsondes [*Rowland et al.*, 1996], and the output of numerical weather prediction models [e.g., *Haack and Burk*,

0048-6604/05/2004RS003112$11.00

Table 1. Mapping Between Domains

	True	Modeled
Data domain	$\mathbf{d}^o$	$\mathbf{d}_i = \mathbf{f}(\mathbf{m}_i)$
Environmental domain	$\mathbf{m}^{true}$	$\mathbf{m}_i$
Usage domain	u^{true}	$u_i = g(\mathbf{m}_i)$

2001] have been viewed as the means for estimating refractivity structures associated with surface-based ducts. In the absence of the refractivity characterization provided by measurements or models, the default (normally resulting in pessimistic predictions of radar range) is to make the assumption of a standard atmosphere.

[4] In the late 1990s the authors and colleagues began looking at the feasibility of inferring low-altitude atmospheric refractivity from radar sea clutter. *Rogers et al.* [2000] demonstrated an algorithm that generated a maximum likelihood (ML) estimate of the evaporation duct height, using radar sea clutter observations at 3.0 GHz, for the case where evaporation ducting is the dominant mechanism of propagation and there is a sufficient clutter-to-noise ratio. To a significant degree this problem has a unique solution at this frequency.

[5] The generation of ML estimators or the maximum a posteriori (MAP) of parameters describing the refractive environment for the case where surface-based ducting is the dominant mechanism of propagation has been addressed by several authors [*Krolik and Tabrikian*, 1998; *Vasudevan and Krolik*, 2001; *Gerstoft et al.*, 2003a, 2003b]. When surface-based ducting is the dominant mechanism of propagation, and both model error and noise are present, the solutions are often nonunique. A weakness of many formulations of ML or MAP estimators, however, is that they contain no information on the certainty of one point vis-à-vis the certainty of others. For cases where the probability in the a posteriori distribution is not concentrated about the MAP or ML estimate (*Gerstoft et al.* [2003a] illustrates this behavior), the ML or MAP solutions may not be the proper answer to the problem; rather, the full solution is the a posteriori probability distribution. *Gerstoft et al.* [2004] explicitly deals with the generation of the a posteriori distributions based on Gaussian assumption of the likelihood function. In that paper, the mismatch between observed and modeled clutter was assumed to be Gaussian (using an ad hoc estimate of the associated covariance), and the result was mapped into the space of the information usage (propagation loss in that instance) so as to provide a measure of the cost of ambiguity and noise.

[6] This paper continues with the theme of *Gerstoft et al.* [2004] of using the Bayesian approach to the generation of a posteriori distribution, but it differs in its implementation. Furthermore, it extends the analysis to examine how well the a posteriori distributions of a scalar usage variable contain the true values of the usage variable.

1.1. Bayesian Framework

[7] An array of observed radar sea clutter observations $\mathbf{d}^o$ is used to generate an estimated "usage" quantity u, such as a signal threshold level. We have no direct mapping from $\mathbf{d}^o$ to u but have "forward" models $f(\cdot)$ and $g(\cdot)$ that can map the ith modeled range and height-dependent refractivity realization $\mathbf{m}^i$ into modeled deterministic clutter ($\mathbf{d}_i$) and usage value (u_i), respectively. The true refractivity ($\mathbf{m}^{true}$) and usage value (u^{true}) are unknown (see Table 1).

[8] Each $\mathbf{m}_i$ is associated with one $\mathbf{d}_i$ and one u_i to form a three-tuple $\{\mathbf{m}_i, \mathbf{d}_i, u_i\} = \{\mathbf{m}, \mathbf{d}, u\}_i$. The a priori probability of $\mathbf{m}_i$ and $\{\mathbf{m}, \mathbf{d}, u\}_i$ are the same, that is, $P(\mathbf{m}_i) = P(\{\mathbf{m}, \mathbf{d}, u\}_i) = P_i$. Bayes rule applied to this problem is

$$P(\mathbf{m}_i|\mathbf{d}^o) = \frac{p(\mathbf{d}^o|\mathbf{m}_i)P(\mathbf{m}_i)}{\sum_{j=1}^{M} p(\mathbf{d}^o|\mathbf{m}_j)P(\mathbf{m}_j)}, \tag{1}$$

where $P(\mathbf{m}_i|\mathbf{d}^o)$ is the a posteriori probability (refining our estimate of $\mathbf{m}$ by adding the information in $\mathbf{d}^o$), and $p(\mathbf{d}^o|\mathbf{m}_i)$ is the conditional probability density of $\mathbf{d}$ given $\mathbf{m}_i$. The forward model $\mathbf{f}(\cdot)$ is embedded in $p(\mathbf{d}^o|\mathbf{m}_i)$. The small p denotes probability density as opposed to a probability ($\mathbf{d}^o$ is generally a continuous quantity). The index of the $\mathbf{m}$ corresponding to the maximum a posteriori estimator is

$$i^{MAP} = \overset{\arg\max}{i}\; P(\mathbf{m}_i|\mathbf{d}^o). \tag{2}$$

The posterior distribution of u is found via the empiric or sample method [*Dudewicz and Mishra*, 1988], which can be realized as

$$P(u < \alpha|\mathbf{d}^o) = \sum_{i=1}^{i=M} P'(u_i), \tag{3}$$

where

$$P'(u_i) = \begin{cases} P(\mathbf{m}_i|\mathbf{d}^o) & \text{for } u_i < \alpha \\ 0 & \text{otherwise.} \end{cases} \tag{4}$$

1.1.1. Common Assumptions

[9] The Bayesian framework does not impose a model for $p(\mathbf{d}^o|\mathbf{m}_i)$. However, it is often modeled as a multivariate Gaussian process [see *Gerstoft et al.*, 2003a]

$$\mathrm{p}(\mathbf{d}^o|\mathbf{m}_i) = \frac{e^{\frac{-1}{2}(\mathbf{f}(\mathbf{m}_i)-\mathbf{d}^o)^T\mathbf{C}^{-1}(\mathbf{f}(\mathbf{m}_i)-\mathbf{d}^o)}}{(2\pi)^{\frac{N}{2}}\det(\mathbf{C})}, \tag{5}$$

with the covariance matrix $\mathbf{C}$ of the form

$$\mathbf{C} = \sigma^2\mathbf{I}. \tag{6}$$

There are at least two reasons why (5) and (6) may not be physically consistent with the nature of this problem:

[10] 1. Contamination of $\mathbf{d}^o$ due to the horizontal variability of the sea clutter radar cross section is expected to be a major component of the mismatch $\mathbf{f}(\mathbf{d}_i) - \mathbf{d}^o$. That would be expected to be a colored process (e.g., a Markov process); thus $\mathbf{C}$ would not have the form of a scaled identity matrix.

[11] 2. The effect of nuisance parameters (i.e., what is not modeled in $\mathbf{m}$ but can be present in $\mathbf{m}^{true}$) on $\mathbf{d}^o$ includes the behavior of horizontal displacements of clutter features relative to where the features (e.g., clutter rings) were the nuisance parameters not present. The evidence of this is illustrated in work by *Gerstoft et al.* [2003a, Figures 8 and 9]. Displacements are not accounted for in equation (5).

1.1.2. Attributes of Implementation of Bayes Rule

[12] We present an inverse method that differs from what is described in section 1.1.1. We use random functions to characterize the mismatch between $\mathbf{f}(\mathbf{m})$ and $\mathbf{d}^o$. Then we incorporate threshold likelihood function. In the context of the preceding discussions, the inversion algorithm has the following attributes.

[13] The probability distribution of $\mathbf{m}$ is represented by $\mathbf{m}_i$ for $i = 1, 2, \subset \ldots M$ samples. The samples are equally likely, that is,

$$P(\mathbf{m}_i) = \frac{1}{M}. \tag{7}$$

Each sample is mapped into one deterministic realization of clutter $\mathbf{d}_i^{det} = \mathbf{f}(\mathbf{m}_i)$ and into the scalar usage variable u_i. Random functions $\Psi_j(\cdot)$ for $j = 1, 2, \ldots N$ map the $\mathbf{d}_i^{det}$ into random replicas $\mathbf{d}_{i,j} = \Psi_j(\mathbf{d}_i^{det})$. That leads to $M \times N$ equally likely tuples of the form $\{\mathbf{m}_{i,j}, \mathbf{d}_{i\ \ ,j}^{det}, \mathbf{d}_{i,j}, u_{i,j}\} = \{\mathbf{m}, \mathbf{d}^{det}, \mathbf{d}, u\}_{i,j}$, where $\mathbf{m}_{i,j} = \mathbf{m}_i$ for $j = 1, 2, \ldots N$, and likewise for $\mathbf{d}_i^{det}$ and u_i.

[14] We implement a thresholded likelihood by defining a sample region S around the observation ($\mathbf{d}^o$) with experimental probability

$$P(\mathbf{d}^o|\mathbf{m}_{i,j}) = \begin{cases} 1 & \text{for } \mathbf{d}_{i,j} \in S \\ 0 & \text{for } \mathbf{d}_{i,j} \notin S. \end{cases} \tag{8}$$

Note that $P(\mathbf{d}^o|\mathbf{m}_{i,j}) = 1$ for $\mathbf{d}_{i,j} \in S$ because there is only one $\mathbf{d}^o$ in S. On the other hand, letting $N_{\mathbf{d}_{i,j}}$ be the number of $\mathbf{d}_{i,j}$ in S leads to

$$P(\mathbf{m}_{i,j}|\mathbf{d}^o) = \begin{cases} \frac{1}{N_{\mathbf{d}_{i,j}}} & \text{for } \mathbf{d}_{i,j} \in S \\ 0 & \text{for } \mathbf{d}_{i,j} \notin S \end{cases} \tag{9}$$

$$= \frac{P(\mathbf{d}^o|\mathbf{m}_{i,j})}{\sum_{i'=1}^{i'=M} \sum_{j'=1}^{j'=N} P(\mathbf{d}^o|\mathbf{m}_{i',j'})}; \tag{10}$$

hence Bayes rule is satisfied for this case where the $\mathbf{m}_{i,j}$ have equal a priori likelihood. The probability of a given $\mathbf{m}_i$ is found by summing over j:

$$P(\mathbf{m}_i|\mathbf{d}^o) = \sum_{j=1}^{j=N} P(\mathbf{m}_{i,j}|\mathbf{d}^o). \tag{11}$$

Finally, the distribution function of u is found as in (3) and (4).

1.2. Inversion Calibration

[15] The behavior of Ψ and S are determined by their nature and parameters used to control them. These ultimately control the shape of the a posteriori distribution. The desired behavior is that the ground truth u^{true} falls between the 0th and 20th percentile levels of a posteriori distribution of u 20% of the time, between the 20th to 80th percentile levels 60% of the time, etc. A trial-and-error process was used to adjust the distribution for the simulation cases. Ideally, a maximum likelihood procedure is where the parameters controlling the inversion are varied so as to maximize the a posteriori probability of u^{true}.

1.3. Usage Scalar *u*(m)

[16] In the case of noise-limited detection, one factor determining whether or not a target can be kept in track is the signal-to-noise (S/N) ratio of the target at points along the track. A robust tracking algorithm will tolerate some dropouts (hits where S/N drops below some threshold value) but will drop a track if a series of drop-outs exceeds some maximum "coasting" distance. An approximate answer as to whether a drop-track event will occur (when all other factors such as the target's radar cross section are taken into account) is the percentile level of the target's S/N dropouts. In this paper, we use a non-system-specific statistic of the propagation loss as our usage variable u. Here $u(\mathbf{m})$ is the 20th percentile level of the two-way propagation loss ($-2L$) for a given environment $\mathbf{m}$ at a height of 5 m over the range interval of 10–60 km. An example of u showing how it relates to propagation loss on the described track is shown in Figure 1.

2. Inversion Algorithm

2.1. Refractivity Model

[17] In the Bayesian paradigm, $p(\mathbf{m})$ is the a priori distribution of models. In this particular instance, it is the distribution of range-dependent refractivity models $\mathbf{m}$. At present we do not (perhaps cannot) express $p(\mathbf{m})$ in closed form. Rather, we implement an $\mathbf{m}$ generator such that an ensemble of draws from the $\mathbf{m}$ generator is a sample representation of $p(\mathbf{m})$. Ideally, it would be

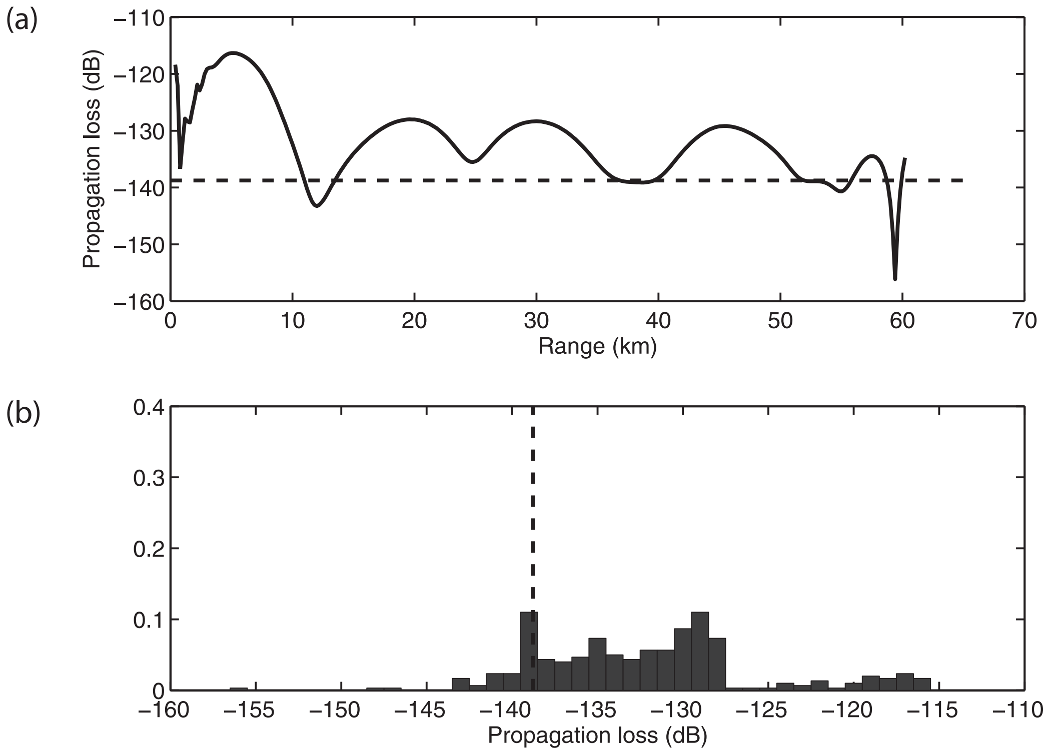

Figure 1. (a) Propagation loss for a typical ducting environment. (b) Histogram for the propagation loss. The dashed line in both plots indicates the 20th percentile. The model is based on the refractivity profile from the Wallops 1998 experiment [*Gerstoft et al.*, 2003a]. See color version of this figure in the HTML.

impossible to distinguish an ensemble of draws from the **m** generator from a representative set of range-dependent refractivity profiles from the true environment. As will be seen at the end of this section, the model falls short of this goal. As will be seen in section 3, however, the **m** generator's weaknesses do not prevent the inversion algorithm from obtaining usable results.

[18] Sixteen observed range-dependent modified refractivity profiles are shown in Figure 2. All were obtained on over-water flights in the vicinity of Wallops Island, Virginia. The first 10 sets of profiles were obtained on 2 May 1998, the next one on 29 April 2000, and the last five on 30 April 2000. All of these are surface-based ducts of the type associated with thermal internal boundary layers. The tops of the trapping layers are typically 20–60 m with the exception of the set on the third position on the bottom row where the negative gradients exist up to 100 m in the first profile.

[19] The four-layer model of the vertical refractivity structure of modified refractivity that is used in the **m** generator is shown in Figure 3. The actual algorithm is described in Appendix A. An important aspect of this model is that the second layer can have positive or negative gradients. It is shown with a positive gradient in Figure 3, a behavior consistent with trapping layer associated with subsidence-driven inversions [*Gossard and Strauch*, 1983, p. 36]. Allowing this range of gradients in the second layer increases the ability of the model to assume shapes consistent with thermal internal boundary layers. A random refractive environment generator or "**m** generator" has been implemented (see Appendix A). This algorithm constructs a range- and height-dependent refractivity structure that (largely) lies within the bounds described in the literature.

[20] Sixteen range-dependent sets of profiles are shown in Figure 4. It is clear that the goal of having the ensemble behavior of the **m** generator resemble that of nature is reasonably achieved. A small inconsistency is that the depths of the ducts are comparable, but the magnitude of the change in refractivity from the value at the surface to the minimum value in the profiles appears to be somewhat larger in the observed profiles than in those produced by the **m** generator. From comparison of (4) to (2), it is observed that the modeled range depen-

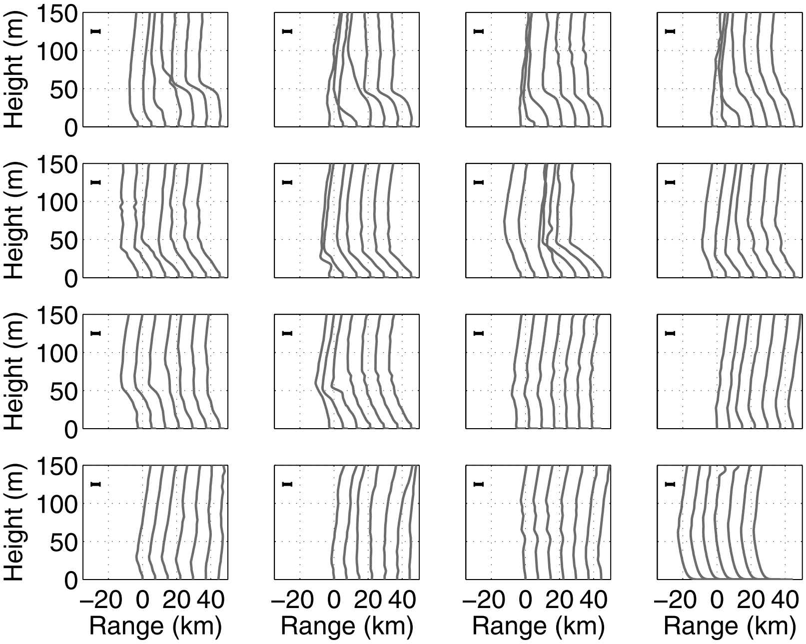

Figure 2. Range-dependent refractivity profiles based on in situ meteorology via helicopter above the Atlantic Ocean in the vicinity of Wallops Island, Virginia. The bar in the top left corner of each plot represents 10 M units. See color version of this figure in the HTML.

dence is somewhat less than that observed in nature. Our experience has shown that allowing some model behavior that is "outside" of reality is more costly than not allowing some model behavior that is within reality, hence the lesser degree of range dependence.

2.2. Generation of Replica Fields

[21] The Advanced Propagation Model (APM) [*Barrios*, 1994, 1997] is used to map the $\mathbf{m}_i$s into propagation loss L as a function of range and height. From *Gerstoft et al.* [2003a], the radar equation for sea clutter in the instance of a range-independent sea clutter radar cross section can be written

$$d^{det}(r_k, \mathbf{m}_i) = -2(\mathbf{m}_i, z_c, r_k) + 10\log(r_k) + C, \tag{12}$$

where each $d^{det}(r_k, \mathbf{m}_i)$ is an element of $\mathbf{d}^{det}$, the term $10\log(r_k)$ for the linear increase in the illuminated areas footprint with respect to range, and C accounts for the range-independent radar cross section and the radar system parameters. In the context of this paper, the superscript "det" denotes a "deterministic" replica in that there is a one-to-one mapping from $\mathbf{m}$ into d for a given C and z_c.

[22] The random function $\Psi_j(\cdot)$ for $j = 1, 2, \ldots N$ maps deterministic replica ($\mathbf{d}_i^{det}$s) into random replicas $\mathbf{d}_{i,j}$s via two independent sequential processes. The first process is a mapping of the range indices. Let $\mathbf{r} = r_1, r_2, \ldots$ be the range indices. We utilize a mapping

$$\mathbf{r} \underset{\text{(random displacement)}}{\overset{\Psi}{\longrightarrow}} \mathbf{r}'. \tag{13}$$

The range displacement vector is developed via a Markov process where the standard deviation of the

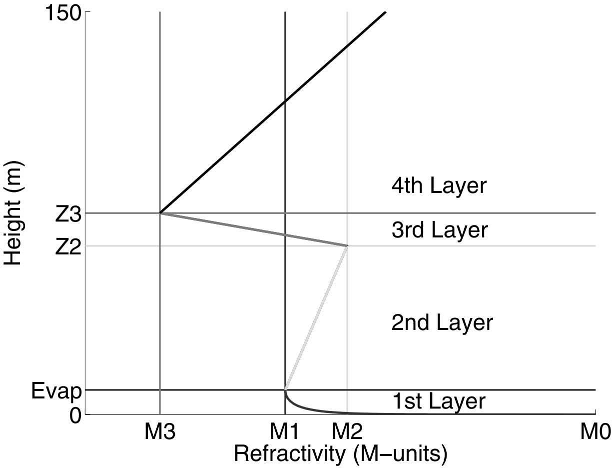

Figure 3. Four-layer model of vertical refractivity profile. See color version of this figure in the HTML.

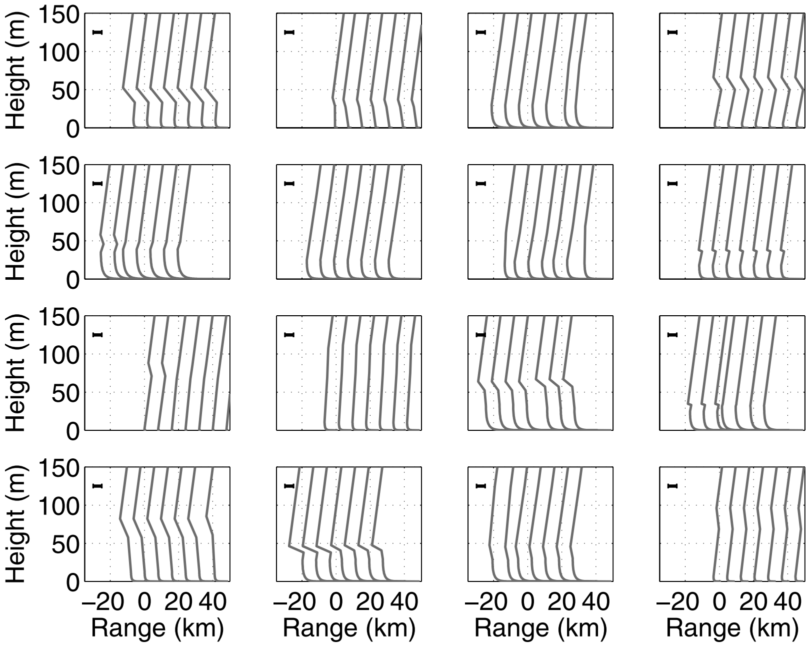

Figure 4. Modeled refractivity fields. The bar in the top left corner of each plot represents 10 M units. See color version of this figure in the HTML.

accumulated shifts at the range of 100 km is 3 km. Next, a random slope ($\frac{\Delta d}{\Delta r}$) based on a zero mean Gaussian random draw is added to the range-displaced modeled clutter array to obtain the second mapping

$$d(\mathbf{r}') \quad \underset{\text{(random slope)}}{\overset{\Psi}{\longrightarrow}} \quad d'(\mathbf{r}'). \tag{14}$$

Over an ensemble of random replicas generated in this manner, the standard deviation of the additive slopes is 10 dB/100 km. We note that ideally, the parameters controlling the behavior of Ψ should be jointly optimized along other parameters controlling the inversion.

[23] Figure 5 shows the deterministic replica field $\mathbf{d}_i^{det}$ (blue curve) and associated random replicas $\mathbf{d}_{ij}$ (red curve). The nature of the slope variations and random displacements are clearly evident.

2.3. Sampling in Vicinity of Observation

[24] Observed clutter data is in the vector $\mathbf{d}^o = \{d_1, d_2, \ldots d_{Nr}\}$, where N_r is the number of ranges. The closeness of fit of each random replica is evaluated using the weighted sum of the mean-removed absolute difference (i.e., a weighted 1 norm)

$$\phi_{i,j} = \phi\left(\mathbf{d}^o, \mathbf{d}_{i,j}\right) = \mathbf{e}_{i,j} \cdot \mathbf{w} \tag{15}$$

$$e_{i,j}(r_k) = \left| d^o(r_k) - \langle \mathbf{d}^o \rangle_r - d_{i,j}(r_k) + \left\langle \mathbf{d}_{i,j} \right\rangle_r \right| \tag{16}$$

$$w(r_k) = \begin{cases} 0 & \text{for} & & r_k < 10 \\ 1 & \text{for} & 10 < & r_k < 20 \\ \frac{150 - r_k}{130} & \text{for} & 20 < & < \leq 150 \\ 0 & \text{for} & 150 < & r_k . \end{cases} \tag{17}$$

The weighting term makes the algorithm most sensitive to clutter that is close to the radar system, with the exception of the closest 10 km. Within 10 km, the

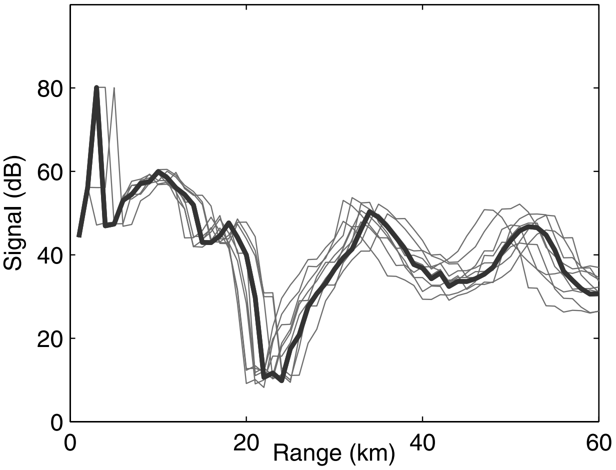

Figure 5. Deterministic replica field $\mathbf{d}^D$ (thick solid curve) and associated random replicas $(\mathbf{d})$. See color version of this figure in the HTML.

grazing angle of the incident radiation is changing rapidly, and the effects of that on σ° have not been incorporated into our modeling [*Rogers et al.*, 2000].

2.4. Modeling Noise Floor Effects

[25] In the preceding discussions, noise floor considerations were not taken into account. It is quite possible for the noise floor to be above the signal level of the clutter (because of insufficient power-aperture-gain product, low wind speeds, etc.). Simulated inversions, including noise floor effects, are implemented by truncating the simulated data and replica fields in the following manner:

[26] 1. The simulated data vector $\mathbf{d}^o = [d_1^o, d_2^o, \ldots]$ is modified by

$$d_i^{o\ \mathrm{Truncated}} = \left\{ \begin{matrix} d_i^o - T & \text{for} & d_i^o > T \\ d_i^o = 0 & \text{for} & d_i^o > T \end{matrix} \right\} \forall i, \tag{18}$$

where T is a threshold value.

[27] 2. The "area" of the data vector is computed

$$A^{\mathbf{d^o}} = \sum_i d_i^{o\ \mathrm{Truncated.}} \tag{19}$$

[28] 3. Each random replica is truncated by determining the value of T that would result in the random replica having its area equal to $A^{\mathbf{d^o}}$. (Note: The threshold values for each random replica are unique.)

[29] The authors note that a more rigorous treatment of modeling the mixture of clutter returns and noise if found in work by *Krolik and Tabrikian* [1998] and *Vasudevan and Krolik* [2001].

2.5. Definition of the a Posteriori Distribution

[30] The a posteriori distribution of $\mathbf{m}$ is generated as described in equations (8) and (10). The remaining question is how to define S. First, we define the threshold value ϵ via

$$\phi_{i,j} \le \epsilon \longrightarrow \mathbf{d}_{i,j} \in S \longrightarrow P\left(\mathbf{d}^o | \mathbf{m}_{i,j}\right) = 1 \tag{20}$$

$$\phi_{i,j} > \epsilon \longrightarrow \mathbf{d}_{i,j} \in S \longrightarrow P\left(\mathbf{d}^o | \mathbf{m}_{i,j}\right) = 0. \tag{21}$$

The value of ϵ is ultimately controlled by an inversion parameter $N^{\max}$, where the relationship between them is

$$\epsilon = \underset{\epsilon}{\arg\max} \left\{ \underset{i}{\arg\max} \sum_{j=1}^{j=N} P\left(\mathbf{d}^o | \mathbf{m}_{i,j}\right) \le N^{\max} \right\}. \tag{22}$$

In other words, ϵ is set such that for the environment $(\mathbf{m}_i)$ corresponding to having the most $\mathbf{d}_{i,j}$s in S, the number of $\mathbf{d}_{i,j}$s in S will be equal to or slightly less than $N^{\max}$. In the inversion runs performed in this paper, $N^{\max} = 0.25\ N$; note, however, that the corresponding value of ϵ differs for each inversion run as it is set by equation (22). Ideally, $N^{\max}$ and the parameters controlling the behavior of Ψ would be jointly optimized.

Table 2. Inversion Runs

	Value
Antenna height, m	31
Polarization	vertical
Beam width, deg	0.4
Beam elevation	horizon

3. Results

[31] All inversion results are based on the radar system parameters of the Space Range Radar (SPANDAR) system operated by the Goddard Space Flight Center at Wallops Island, Virginia [*Stahl and Crippen* 1994]. The parameters from the SPANDAR radar that are important in our work are given in Table 2. The true refractivity $(\mathbf{m}^{true})$ and usage value (u^{true}) are unknown (see Table 2). Inversions using real clutter data are based on SPANDAR data from the Wallops 1998 measurement campaign [*Rogers et al.*, 2000].

3.1. Simulation Results Using Synthesized Clutter

[32] A simulated inversion run begins with a call to the $\mathbf{m}$ generator to generate the "real" environment, $\mathbf{m}_{real}$. As a random draw, this $\mathbf{m}_{real}$ should not be identically equal to any previous or future draws from the $\mathbf{m}$ generator. Here $\mathbf{m}_{real}$ is mapped into a deterministic realization of clutter $\mathbf{d}^D = [d^D{}_1, d^D{}_2, \ldots]$, as well as into $u(\mathbf{m}_{real})$. A corrupted realization of clutter ($\mathbf{d}^o = [d^o{}_1, d^o{}_2, \ldots]$) is generated by the process

$$N = [n_1, n_2, \ldots] \tag{23}$$

$$n_1 = 0 \tag{24}$$

$$n_{i+1} = n_i + \gamma_i \tag{25}$$

$$\gamma_i \sim \mathcal{N}\left(0, \sigma_\gamma^2\right) \tag{26}$$

$$\mathbf{d}^o = \mathbf{d}^D + N, \tag{27}$$

where γ_i is an independent draw from a zero mean Gaussian random number generator,and the resulting vector N is a Markov chain. Note that the noise added here differs from that described in section 2.2 in that the latter is simply a slope. The purpose of adding the colored noise to $\mathbf{d}^D$ is to simulate the effects of range-

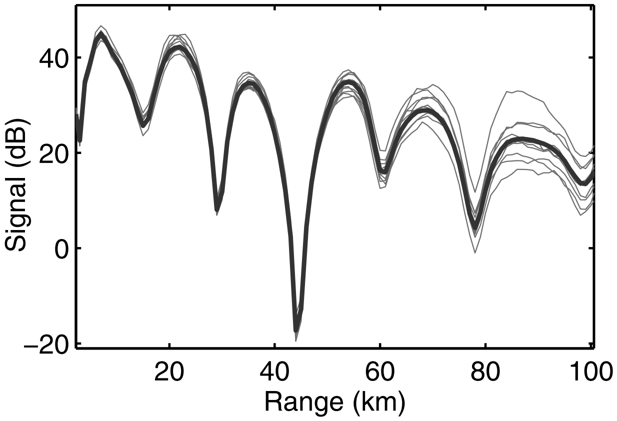

Figure 6. Uncorrupted synthesized clutter $\mathbf{d}^D$ and realizations of corrupted clutter about it that are used as inputs to the inversion algorithm for simulation cases. Corrupting effects are based on the assumption of the sea clutter radar cross section σ° behaving as a Markov process with respect to range. See color version of this figure in the HTML.

varying sea clutter radar cross section. Realizations of $\mathbf{d}^o$ about $\mathbf{d}^D$ corresponding to one $\mathbf{m}$ are shown in Figure 6.

[33] Results using synthesized clutter observations where the effects of system noise are not being considered are shown in Figure 7. On the left of the plot, it can be seen that the a priori cumulative distribution of u with the 5th, 20th, 80th, and 95th percentile levels delineated. To the right are 20 independent inversion runs, all corresponding to ducting conditions. Here u_{real} is shown with the symbol *. Ideally, u_{real} would lie below the 5th percentile level 5% of the time, between the 20th and 80th percentile levels 60% of the time, and so on. While that is not precisely the case, it is clear that given the limited number of cases shown in the picture, the "containment" of u_{real} appears to be roughly correct.

3.2. Real Data Results Using Inversion Method Calibrated in Simulation

[34] The Wallops 1998 propagation experiment [*Stapleton et al.*, 2001] took place over 5 weeks in the April–May time frame of that year. The experimental equipment included a microwave propagation measurement system (MPMS) with receivers at a location on the beach at Wallops Island and transmitting equipment located on a boat named the *Sea Lion*. The system on the *Sea Lion* transmitted in S, C and X bands. In each band, the output of the transmitters was switched through horn antennas mounted on a mast so as to rapidly vary the height of the transmitters. For each outbound run of the *Sea Lion*, a matrix of propagation loss values was generated corresponding to the ranges covered by the boat and the heights of the transmitters (nominally, 1–9 m).

[35] Experimental events were organized around outbound runs of the *Sea Lion* on the 150° (true north) radial

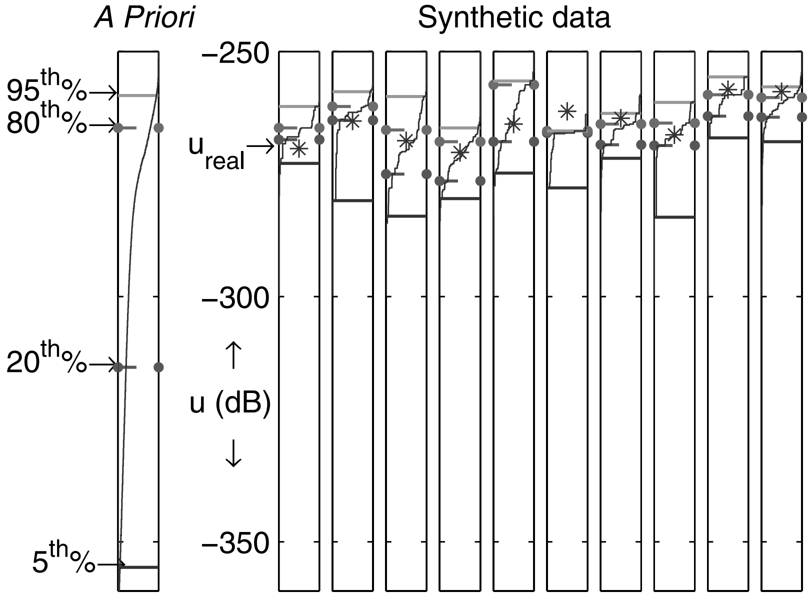

Figure 7. Simulated inversions. Left plot is a priori distribution of u with 5th, 20th, 80th, and 95th levels shown. To the right are the a posteriori distributions and associated levels. See color version of this figure in the HTML.

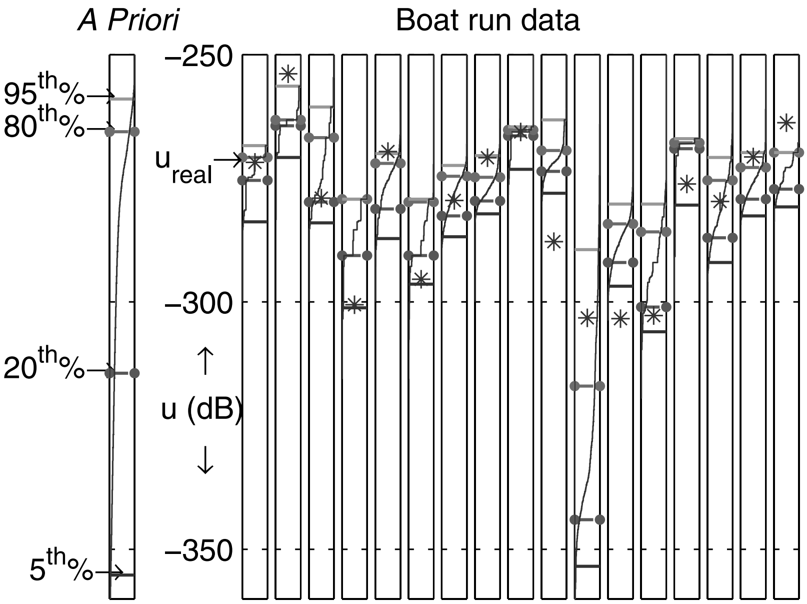

Figure 8. Real data inversions with the input to the inversion algorithm from radar clutter observed via SPANDAR and the u^{true} values taken from in situ measurements of propagation loss via the MPMS system. The system settings are the same as for Figure 7. See color version of this figure in the HTML.

from the transmitting site. Boat runs would begin at a nominal range of 5 km and would terminate at ranges up to 60 km. Several means were employed to obtain ground truth refractivity data; these included helicopter soundings, rocketsondes, and using data from meteorological buoys to characterize the surface layer. There were a total of total 41 events. Using the available data sources (e.g., soundings via rocket or helicopter, radar clutter maps, and data from MPMS) led to the human determination that for 20 of the events, surface-based ducting was the dominant mechanism of propagation. Of the 20 events, 17 events included clutter observations where SPANDAR's maximum range was greater than 100 km.

[36] For each of the 17 events, the data needed to compute u as described in section 1.3 were extracted from the data recorded using MPMS. Radar clutter maps from SPANDAR, corresponding as close in time as possible to the center time of the boat runs, were then determined. The clutter from these clutter maps were then used as inputs to the inversion algorithm. Figure 8 shows the results using the inversion algorithm when the settings used in the generation of Figure 7 are employed. In these cases, 5/17 (30%) of the data are outside of the 5th to 95th percentile interval, and only 4/17 (24%) are within the 20th to 80th percentile interval (the values should be 10% and 80%, respectively). Further adjustments to the parameters affecting the inversion (i.e., $P_e^{\max}$ and those affecting Ψ) yielded only limited improvement. Figure 9 shows such a case: We still have 5/17 (30%) of the data are outside of the 5th to 95th percentile interval; however, 7/17 (41%) are within the 20th to 80th percentile interval.

[37] The disparity between the real data cases and simulation is likely explained as being the combination of factors that include the following.

[38] 1. The noise injected to create the corrupted realizations of clutter pictured in Figure 6 does not properly account for the real-world random processes affecting the clutter and modeling errors that real data cases expose.

[39] 2. The a priori distribution of $\mathbf{m}$ is different from the distribution (the unknown) $\mathbf{m}^{true}$ over the 17 cases.

3.3. Simulations and Real Data Cases That Include Noise Floor Effects

[40] Low wind speeds, reduced radar power, reducing the size of the radar's antennas, and so on reduce the clutter-to-noise ratio (C/N). If the inversion algorithm is working correctly, decreasing C/N should result in widening the a posteriori distribution as more information in the clutter return is being obscured by the system noise. At sufficiently low C/N values, the a posteriori distribution should be identical to the a priori distribution.

[41] Figure 10 shows synthesized observations (blue curve) and best fitting replicas (red curve) for two

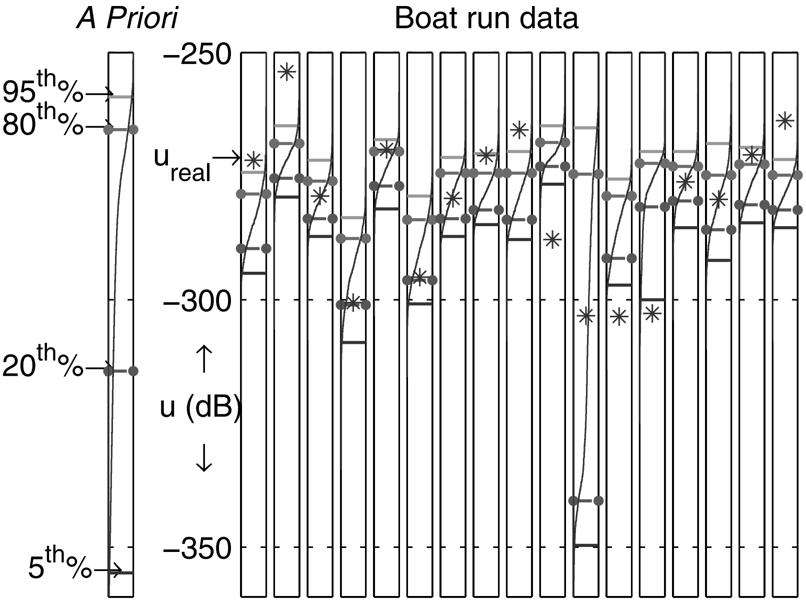

Figure 9. Same as Figure 8 but with system settings optimized for the real data cases. See color version of this figure in the HTML.

simulated environments where the threshold T (see section 2.4) is varied from -320 to -270. First consider the truncated data vector (the top curve in each plot): At $T = -320$, there is very little evidence of the noise floor in the (synthesized) clutter (the noise in these plots would be a straight line at 0 dB on the abscissa). At $T = -290$, there is no observable clutter beyond 25 km in the series of plots on the left side. In the plots on the right, the T value where the same behavior occurs is -280. At $T = -270$, the thresholding has completely obscured the signature of the propagation. Now consider the family of deterministic replicas that are shown in red (offset 40 dB from the synthesized clutter). These are the (nontruncated) deterministic replicas $\mathbf{d}^{det.}$ that are associated with the a posteriori distributions of $\mathbf{m}$ and u. For the case on the left, it is clear that the replicas have the major features of the observed data at $T = -320$, less so at $T = -310$, but very poor feature correspondence at lower levels. For the case on the right, reasonable gracefully degrading feature correspondence is found all the way down to the $T = -280$ level.

[42] Figure 11 is similar to Figure 10 except (1) the two examples are from the 17 real data cases used to generate Figure 8, and (2) the title of each subplot is the threshold level above the noise by which the observed clutter signal is reduced. In the top row are two examples where the clutter data has not been thresholded. The clutter peaks in the range of 25–50 km are (nominally) 25 dB above the noise floor, and the replicas largely exhibit the behavior of the observed clutter. At 30 dB of thresholding, no clutter is seen beyond 15 km or so, and

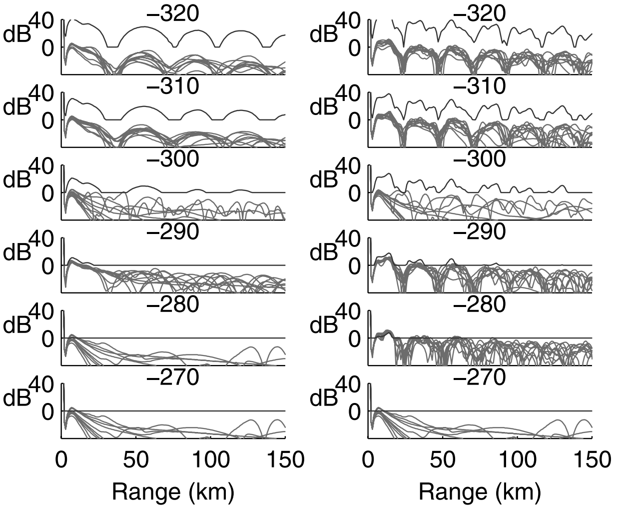

Figure 10. Effect of noise floor on fit of modeled to simulated observed clutter for two cases. Individual graph titles are the T level (see section 2.4). The top curve (blue) in each plot is the synthesized clutter return with respect to the noise floor at 0 dB. The series of curves at the bottom of each graph are the deterministic replicas corresponding to the 10 most likely modeled environments. See color version of this figure in the HTML.

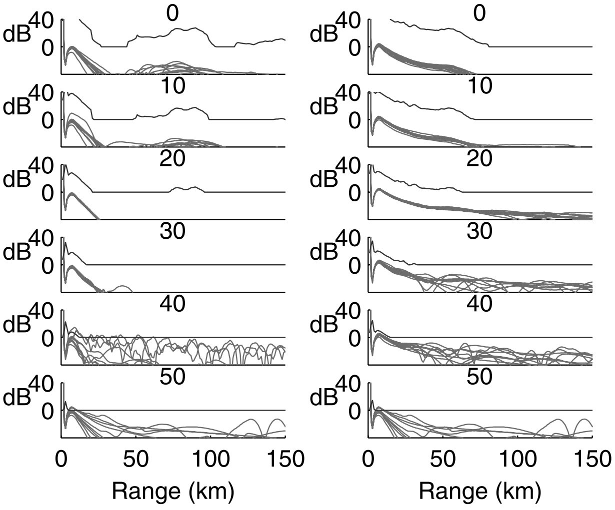

Figure 11. Effect of noise floor on fit of modeled to (simulated) observed clutter for two real data cases. See color version of this figure in the HTML.

the replicas show behavior that is unlike the observed clutter.

[43] Figure 12 has summary graphs for 100 simulation cases (left) and the real data cases. On the left, the abscissa is T. On the right, the abscissa is the threshold above noise level. The ordinate in each plot is the interval between the 20th and 80th percentile levels of a posteriori distribution of u. For the simulation cases, the abrupt transition from a narrow a posteriori distribution to the width of the a priori distribution occurs at approximately $T = -290$. The transition in the real data cases occurs at a threshold increase of 30 dB. The reason the maximum interval width in the real data plot is less than that in the plot based on the simulation cases is that some of the real data cases were over range intervals smaller than the 10–60 km interval used for the simulation cases.

[44] A final note is that the 17 cases from Wallops 1998 are for weak surface-based duct cases. *Gerstoft et al.* [2003a] present data taken with the SPANDAR that shows peak clutter levels in the 25–50 km interval of 45–55 dB above system noise for a strong ducting event. (Note that we do not possess u values for the 1998 data). We would expect that for such cases, the curve in the right-hand plot of Figure 12 would be displaced approximately 20 dB to the right.

[45] This analysis brings up two points.

[46] 1. As described by *Rogers et al.* [2000], a shipboard radar system having a 2.9 m antenna (but otherwise similar to SPANDAR), would have a 20 dB lower C/N ratio than SPANDAR under otherwise similar environmental conditions. That implies that for the cases reported here, a shipboard system that was similar to SPANDAR (except with regard to its antenna) would be sufficient (but just sufficient) to use the technique described here.

[47] 2. The information content of the clutter is both dependent on both the environmental state (unknown a priori) and is system dependent. Because of those dependencies, it is clear that the certainty of the solutions is a dynamic quantity, preferably one that is directly inferred from the data.

4. Summary

[48] The a posteriori distribution is the appropriate solution to the inverse problem. However, it is quite easy to use modeling assumptions such that the uncertainty of the a posteriori solution is underestimated. For the problem of determining propagation loss from radar clutter, we first determine properly scaled a posteriori distributions and then evaluate their goodness in whether they properly contain ground truth.

[49] In this paper, random functions are used to characterize the mismatch between model and observation, in conjunction with a threshold likelihood function. These might be thought of as admitting a larger set of mismatch behaviors than are allowed by the assumption of additive Gaussian noise. We cannot yet say this is better than employing a Gaussian assumption; rather, it is an alternate approach that is no less physically justified than the Gaussian approach.

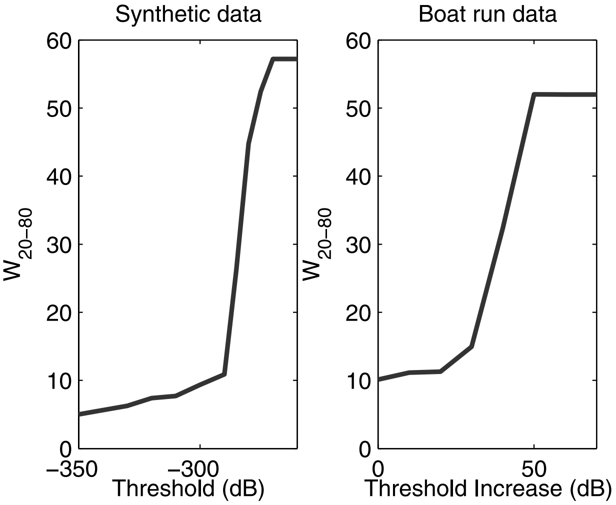

Figure 12. Summary graphs of the effects of noise floor for (left) 100 simulated and (right) the 17 real data cases. On the left, the abscissa is T (see section 2.4), and on the right, the abscissa is the threshold above noise level. The ordinate in each plot is the interval between the 20th and 80th percentile levels of a posteriori distribution of u. See color version of this figure in the HTML.

[50] In simulation, we demonstrated the ability to generate what appears to be correctly adjusted a posteriori distributions of the usage variable u. The statistic u is the 20th percentile level of the two-way propagation loss at a height of 5 m over the range interval 10–60 km. Achieving that result required trial-and-error adjustment of parameters affecting the behavior of the random functions and the thresholded likelihood functions that are part of the inversion algorithm. When the inversion algorithm is implemented with real data, the a posteriori distributions of the usage variable are too narrow; they do not fully capture the uncertainty in the predictions.

[51] The effect of the noise floor on inversion results is also addressed. In both simulation and real data cases, it is seen that the width of the a posteriori distribution widens very quickly when the peak clutter returns in the interval of 25–50 km, dropping to values less than about 15 dB above the noise floor. The fact that the a posteriori distribution behaves in this manner is a desired attribute of the inversion algorithm.

Appendix A: M Generator

[52] An iteration of the **m** generator results in the construction of a vertical refractivity profile as defined in equation (A1), based on a sequence of five draws from uniform (U) random number generators as given in equations (A2)–(A9), with limits on the random number generation being given in equations (A10)–(A13). These equations constitute an ad hoc means of achieving ensemble behavior of the **m** generator that is consistent with the following.

[53] 1. The first layer uses the form of the neutral evaporation duct described by *Paulus* [1990] and terminates at the evaporation duct height z_1. For the case where the slope in the second layer is 0.13 M units/m (M units are the refractive index multiplied by 10^6 and then corrected for Earth curvature), the profile of the first and second is approximately what would be expected with an unstable surface layer topped by a mixed layer.

[54] 2. The second layer can accommodate a large range of slopes. For a mixed layer between an unstable surface layer and a stable inversion, *Gossard and Strauch* [1983] have shown that the gradient should be approximately 0.13 M units/m, and observations generally agree with the notion that as the thickness of the mixed layer increases, the tendency toward the 0.13 M units/m increases. In the model used here, gradients c_1 in the range −0.2 to 0.3 M units/m are allowed when the top of the second layer is 50 m or less. The former of the limits is consistent with containing the slopes shown in Figure 2; the latter allows effective Earth radius factor (k factor) [*Hall*, 1989], which can account for subrefractive cases of the kind discussed by *Goldhirsh and Dockery* [2001].

[55] 3. We allow gradients c_2 in the range −3 to 0.13 M units/m in the third layer. This allows the third layer to accommodate slopes that are observed in strongly stable capping inversions [*Rogers*, 1998].

[56] All this leads to the following equations:

$$M(z) = \begin{cases} a_1(z - z_1\log(z\cdot c_0)) & z < z_1 \\ M(z_1) + c_1\cdot(z - z_1) & z_1 < z < z_2 \\ M(z_2) + c_2\cdot(z - z_2) & z_2 < z < z_3 \\ M(z_3) + c_3\cdot(z - z_3) & z_3 < z \end{cases} \tag{A1}$$

$$z_1 \sim U(1, \min[(z_2 - 1), 40]) \tag{A2}$$

$$z_2 = 20 + (z_3 - 21)\cdot\sqrt{v} \tag{A3}$$

$$v \sim U(0,1) \tag{A4}$$

$$z_3 \sim U(30, 125) \tag{A5}$$

$$c_0 = 1/\left(1.5\cdot 10^{-4}\right) \approx 6670 \tag{A6}$$

$$c_1 \sim U\left(c_1^{\min}, c_1^{\max}\right) \tag{A7}$$

$$c_2 \sim U\left(c_2^{\min}, c_2^{\max}\right) \tag{A8}$$

$$c_3 = 0.118 \tag{A9}$$

$$c_1^{\min} = \begin{cases} -0.2 & z_2 < 50\text{ m} \\ a_1 - a_2 e & z_2 > 50\text{ m} \end{cases} \tag{A10}$$

$$c_1^{\max} = \begin{cases} 0.315 & z_2 < 50\text{ m} \\ a_1 + a_3 e & z_2 > 50\text{ m} \end{cases} \tag{A11}$$

$$c_2^{\min} = \begin{cases} -3 & z_2 < 50\text{ m} \\ a_1 - a_4 e & z_2 > 50\text{ m} \end{cases} \tag{A12}$$

$$c_2^{\max} = a_1 \tag{A13}$$

$$e = \exp\left[-\max\left(0, \frac{z_2 - 50}{a_5}\right)\right] \tag{A14}$$

$$\begin{aligned} a_1 &= 0.13 \\ a_2 &= 0.33 \\ a_3 &= 0.18 \\ a_4 &= 3.13 \\ a_5 &= 17.9 \end{aligned}$$

[57] M, e, and v are dimensionless, all zs are in meters, and all cs and as are in (meters)$^{-1}$. The variable z_1 is the evaporative duct height.

[58] The ensembles of profiles in Figure 2 demonstrates range dependency that is sometimes abrupt in nature. A limited degree of range dependency is empirically introduced into the **m** generator in the following manner. Changes in the profile occur with 1/32 probability at each kilometer. This means that the occurrences of change is a Poisson process where the mean horizontal distance between changes is 32 km. When a change occurs, we empirically do the following updates: z_3 is allowed to vary uniformly by ±10%, and z_2 is allowed to vary by 10% in the same direction as z_3. The evaporation duct height is allowed to change uniformly by ±20%, and the value of M at the top of the second and third layers is allowed to vary independently ±5 M units.

Notation

$\mathbf{m}$	modeled range- and height-dependent refractivity.
$\mathbf{f}$	forward model mapping refractivity into clutter.
$\mathbf{L}$	propagation loss (dB).
M	number of deterministic models.
N	number of random realizations per deterministic model.
u	parameter of interest, here 20th percentile level of $-2L$.
$\mathbf{d}^o$	observed or synthesized radar clutter.
$\mathbf{d}_i^D$	deterministic clutter replica.
$\mathbf{d}_{i,j}$	random clutter replica.
S	sampling region used in thresholded likelihood.
ϵ	threshold of $\phi_{i,j}$ defining sample region about $\mathbf{d}^o$.
ϕ	goodness of fit of $\mathbf{d}_{i,j}$ to $\mathbf{d}^o$.
$N^{\max}$	ceiling value for the number of random replicas associated with the replicas whose "distance" to the observation **d** is less than ϵ.ith deterministic
$P(\mathbf{m}_i)$	a priori probability of $\mathbf{m}_i$.
$P(\mathbf{d}^o\|\mathbf{m}_{i,j})$	conditional probability of $\mathbf{d}^o$ given $\mathbf{m}_{i,j}$.
$P(\mathbf{m}_{i,j}\|\mathbf{d}^o)$	conditional probability of $\mathbf{m}_{i,j}$ given $\mathbf{d}^o$.

[59] **Acknowledgment.** The Office of Naval Research, codes 321 and 322, supported this research.

References

Barrios, A. E. (1994), A terrain parabolic equation model for propagation in the troposphere, *IEEE Trans. Antennas Propag.*, *42*(1), 90–98.

Barrios, A. E. (1997), Advanced propagation model, in *Proceedings of the 1997 Battlespace Atmospherics Conference 2–4 December 1997*, *Tech. Doc. 2989*, edited by K. D. Anderson and J. H. Richter, pp. 483–490, Space and Nav. Warfare Syst. Cent., San Diego, Calif.

Dudewicz, E. J., and S. N. Mishra (1988), *Modern Mathematical Statistics*, John Wiley, Hoboken, N. J.

Gerstoft, P., L. T. Rogers, J. L. Krolik, and W. S. Hodgkiss (2003a), Inversion for refractivity parameters from radar sea clutter, *Radio Sci.*, *38*(3), 8053, doi:10.1029/2002RS002640.

Gerstoft, P., L. T. Rogers, W. S. Hodgkiss, and L. J. Wagner (2003b), Refractivity estimation using multiple elevation angles, *IEEE J. Oceanic Eng.*, *28*(3), 513–525.

Gerstoft, P., W.S. Hodgkiss, L.T. Rogers, and M. Jablecki (2004), Probability distribution of low-altitude propagation loss from radar sea clutter data, *Radio Sci.*, *39*, RS6006, doi:10.1029/2004RS003077.

Goldhirsh, J., and G. D. Dockery (2001), K factor statistics for subrefraction in the mid-Atlantic coast of the United States, *Radio Sci.*, *36*(6), 1425–1438.

Gossard, E. E., and R. G. Strauch (1983), *Radar Observations of Clear Air and Clouds*, Elsevier, New York.

Haack, T., and S. D. Burk (2001), Summertime marine refractivity conditions along coastal California, *J. Appl. Meteorol.*, *40*(4), 673–687.

Hall, M. P. M. (1989), *Radiowave Propagation*, Peter Peregrinus, London.

Hitney, H. V., J. H. Richter, R. A. Pappert, K. D. Anderson, and G. B. Baumgartner (1985), Tropospheric radio propagation assessment, *Proc. IEEE*, *73*, 265–283.

Krolik, J. L., and J. Tabrikian (1998), Tropospheric refractivity estimation using radar clutter from the sea surface, in *Proceedings of 1997 Battlespace Atmospherics Conference*, *Tech. Rep. 2989*, edited by K. D. Anderson and J. H. Richter, pp. 635–642, Space and Nav. Warfare Syst. Cent., San Diego, Calif.

Liu, W. T., K. B. Katsaros, and J. A. Businger (1979), Bulk parameterization of air-sea exchanges of heat and water vapor including molecular constraints on the interface, *J. Atmos. Sci.*, *36*, 1722–1735.

Paulus, R. A. (1990), Evaporation duct effects on sea clutter, *IEEE Trans. Antennas Propag.*, *38*(11), 1765–1771.

Rogers, L. T. (1998), Demonstration of an efficient boundary layer parameterization for unbiased propagation estimation, *Radio Sci.*, *33*(6), 1599–1608.

Rogers, L. T., C. P. Hattan, and J. K. Stapleton (2000), Estimating evaporation duct heights from radar sea clutter, *Radio Sci.*, *35*(4), 955–966.

Rowland, J. R., G. C. Konstanzer, M. R. Neves, R. E. Miller, J. H. Meyer, and J. R. Rottier (1996), SEAWASP: Refractivity characterization using shipboard sensors, in *Proceedings of Battlespace Atmospherics Conference Tech. Doc. 2938*, edited by K. D. Anderson and J. H. Richter, pp. 155–164, Nav. Command, Control and Ocean Surveillance Cent., San Diego, Calif.

Stahl, R. W., and D. A. Crippen (1994), An experimenter's guide to the NASA Atmospheric Sciences Research Facility, report, Wallops Flight Facility, NASA Goddard Space Flight Cent., Wallops Island, Va.

Stapleton, J., D. Shanklin, V. R. Wiss, T. Nguyen, E. Burgess, W. Thornton, and T. Brown (2001), Radar propagation modeling assessment using measured refractivity and directly sensed propagation ground truth—Wallops Island, VA 2000, *Tech. Rep. NSWCDD/TR-01/132*, Nav. Surface Warfare Cent., Dahlgren, Va.

Vasudevan, S., and J. L. Krolik (2001), Refractivity estimation from radar clutter by sequential importance sampling, *IEEE Int. Conf. Acoust. Speech Signal Process.*, *5*, 2905–2908.

P. Gerstoft, Marine Physical Laboratory, University of California, San Diego, La Jolla, CA 92093-0238, USA. (gerstoft@ucsd.edu)

M. Jablecki and L. T. Rogers, Atmospheric Propagation Branch, SPAWAR Systems Center, San Diego, CA 92152, USA. (trogers@spawar.navy.mil)